



# CHORUS

This is the accepted manuscript made available via CHORUS. The article has been published as:

## Visualizing Anisotropic Oxygen Diffusion in Ceria under Activated Conditions

Liang Zhu, Xin Jin, Yu-Yang Zhang, Shixuan Du, Lei Liu, Tijana Rajh, Zhi Xu, Wenlong Wang, Xuedong Bai, Jianguo Wen, and Lifan Wang

Phys. Rev. Lett. **124**, 056002 — Published 5 February 2020

DOI: [10.1103/PhysRevLett.124.056002](https://doi.org/10.1103/PhysRevLett.124.056002)

# Visualizing Anisotropic Oxygen Diffusion in Ceria under Activated Conditions

Liang Zhu,<sup>1,2,\*</sup> Xin Jin,<sup>1,2,\*</sup> Yu-Yang Zhang,<sup>2,†</sup> Shixuan Du,<sup>1,2,5</sup> Lei Liu,<sup>3,‡</sup> Tijana Rajh,<sup>4</sup>  
Zhi Xu,<sup>1,2,5</sup> Wenlong Wang,<sup>1,2,5</sup> Xuedong Bai,<sup>1,2,5,§</sup> Jianguo Wen,<sup>4,||</sup> Lifeng Wang<sup>1,4,¶</sup>

<sup>1</sup>Beijing National Laboratory for Condensed Matter Physics, Institute of Physics,  
Chinese Academy of Sciences, Beijing 100190, China

<sup>2</sup>School of Physical Sciences and CAS Center for Excellence in Topological Quantum Computation,  
University of Chinese Academy of Sciences, Beijing 100190, China

<sup>3</sup>Department of Materials Science and Engineering, College of Engineering, Peking University, Beijing 100871, China

<sup>4</sup>Center for Nanoscale Materials, Argonne National Laboratory, Lemont, IL 60439, USA

<sup>5</sup>Songshan Lake Materials Laboratory, Dongguan, Guangdong 523808, China

Oxygen reactivity plays a key role in the performance of ceria-based catalysts. Aberration-corrected transmission electron microscopy and molecular dynamics simulations were used to study the oxygen atom diffusion in ceria under activated conditions. Reactive oxygen atom and its real-time diffusion were visualized. The interplay between cerium and oxygen atoms originating from a Coulomb interaction was revealed by the out-of-plane buckling of cerium atoms associated with oxygen transport. Anisotropic oxygen atom diffusion that depends on crystal orientations was discovered, demonstrating a preferential [001] crystallographic diffusion pathway. These findings reveal prospects for applications of anisotropic orientation-relevant fluorite-structured oxides.

Cerium oxide ( $\text{CeO}_2$ ), also known as ceria, is a typical oxide catalyst [1-3] that has been extensively investigated in the photocatalytic water splitting for hydrogen production [4] and solid-oxide fuel cells for energy storage [5]. Recyclable release and storage of oxygen atoms is the key process for all of these applications [6]. The formation of oxygen vacancies and the migration of oxygen atoms under external stimuli serve as the basis for functional oxide materials and related devices [7]. Real-time visualization of active oxygen vacancies and the exploration of oxygen diffusion pathways on the atomic scale will give rise to the deep understanding of the structure-property relationships, eventually facilitating the control of catalytic processes [8-10].

The structural characterization using transmission electron microscopy (TEM) reveals the key phenomena for ceria redox process, for example, varied surface reconstructions upon the Ce reduction from  $\text{Ce}^{4+}$  to  $\text{Ce}^{3+}$  [11,12]. However, real-time visualization of dynamic oxygen atoms with spatial and, in particular, elementary resolution was a challenge due to aberration of the objective lens. Previously reported negative spherical aberration-corrected TEM suggests that atomic resolution in oxides is promising, as demonstrated in  $\text{SrTiO}_3$  [13]. For functional oxides under activated conditions, advanced methods with the enhanced contrast of oxygen

atoms are required for the atom motion tracking and quantitative measurements. Here, taking ceria, the fluorite-structured catalyst, as a model system, we demonstrate that dynamic oxygen diffusion and its anisotropic character can be directly visualized using the aberration-corrected TEM. The real-time interplay between the cerium cationic lattice rearrangement and the anisotropic diffusion of oxygen atoms is unveiled at the sub-angstrom resolution. The combined study by high-resolution TEM characterizations, density functional theory calculations and molecular dynamics simulations presents a powerful tool for understanding the reactive nature of oxygen atoms in catalysts at the atomic scale.

$\text{CeO}_2$  under the ambient condition has a fluorite structure. We apply the aberration-corrected TEM to determine the structure of  $\text{CeO}_2$  nanoparticles in the ultra-high vacuum system. The details are provided in Fig. 1 in the Supplemental Materials [14]. Under the illumination of the 200 kV accelerated electron, pristine fluorite-structured  $\text{CeO}_2$  transits to  $\text{Ce}_2\text{O}_3$  with a bixbyite structure (space group: Ia3) [35,36]. The atomic schematic of fluorite  $\text{CeO}_2$  and bixbyite  $\text{Ce}_2\text{O}_3$  is shown in Fig. 1(a). Especially, in the bixbyite structure Ce atoms split into d-site and b-site types according to the different coordination with O atoms and vacancies. All

atoms slightly deviate from sites in the cubic unit of the

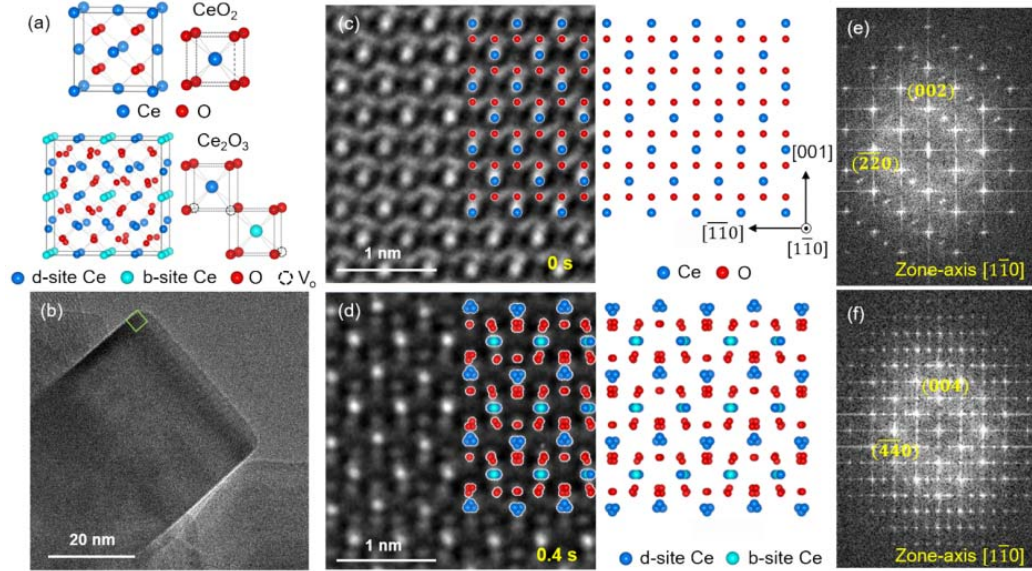


FIG. 1. Atomic resolution TEM imaging of the structural evolution in ceria. (a) Atomic configurations of  $\text{CeO}_2$  (top half) and  $\text{Ce}_2\text{O}_3$  (bottom half). (b) Low-magnification TEM image of  $\text{CeO}_2$  nanoparticle. (c), (d) Snapshot TEM images of the near-edge area in the nanoparticle viewed along the  $[1\bar{1}0]$  crystallographic direction superposing with relaxed atomic configurations of  $\text{CeO}_2$  and  $\text{Ce}_2\text{O}_3$ . Bright and gray spots in TEM images correspond to Ce and O atom columns, respectively. (e), (f) Diffraction pattern for (c) and (d).

fluorite structure. Figure 1(b) shows the overview TEM image of a ceria nanoparticle. With a typical imaging beam flux on the order of  $10^4 \text{ e}/\text{\AA}^2\cdot\text{s}$ , the 200 kV accelerated incident electrons transfer energy up to 33 eV to O atoms in  $\text{CeO}_2$ , which is beyond the previous estimate of the threshold displacement energy (about 27 eV) [37], enabling the observation of the fluorite-bixbyite structure transition via the radiolysis effect. By adjusting the beam flux, release and acquisition of oxygen atoms in nanoparticles can be initiated repeatedly. Figures 1(c) and 1(d) show snapshot TEM images of the near-edge area of the nanoparticle during the radiolysis. We took the view along the  $\langle 110 \rangle$  crystallographic direction so that Ce and O atom columns are well separated and can thus be easily distinguished for both fluorite- and bixbyite-ceria. Atomic models of fluorite- $\text{CeO}_2$  and bixbyite- $\text{Ce}_2\text{O}_3$  are superposed on the TEM images, highlighting both Ce and O atomic positions. Corresponding diffraction patterns of the TEM images as shown in Figs. 1(e) and 1(f) further verify the structures.

To trace the diffusion path of O atoms in ceria, sequential TEM images with a time interval of 0.2 s were recorded (Figs. 2(a)–(d)) to capture intermediate states during reduction (fluorite  $\text{CeO}_2$  to bixbyite  $\text{Ce}_2\text{O}_3$ ). The interplay

between cerium and oxygen atoms has been revealed. When focusing on the O atom column (black arrow), the out-of-plane buckling of O atoms along the  $[001]$  direction evolves during the reduction. Displacement of the spot for the oxygen column is up to  $\sim 40 \text{ pm}$ . The local intensity of the spot increases as shown in the sequential TEM images (Figs. 2(a)–(d), also see Fig. 2 in the Supplementary Materials [14] for more details), indicating the evolution of the O atom concentration in this column. Moreover, the nearest neighboring Ce atom columns (two blue arrows) show the simultaneous out-of-plane buckling clearly. Note that the distance between oxygen and its nearest cerium atom in fluorite- $\text{CeO}_2$  is measured to be  $\sim 2.4 \text{ \AA}$ . When a diffusing O atom travels across the Ce plane, the distance between Ce and O atoms decreases to  $\sim 1.9 \text{ \AA}$ . Thus, the electrostatic force on the Ce atoms get enhanced dramatically because of the charge re-distribution, causing the out-of-plane buckling of Ce atoms and the volume expansion of  $\text{CeO}_2$  cell (see video and Fig. 3 in Supplementary Materials [14] for more details). While electron reduction is the driving force for the O atom migration, the accompanying lattice perturbation of surrounding Ce atoms provides additional resistance, hindering the diffusion of O atoms [38]. More importantly,

when considering the lattice symmetry, the optimized oxygen diffusion path with the lowest diffusion

barrier may exist while the accompanying perturbation

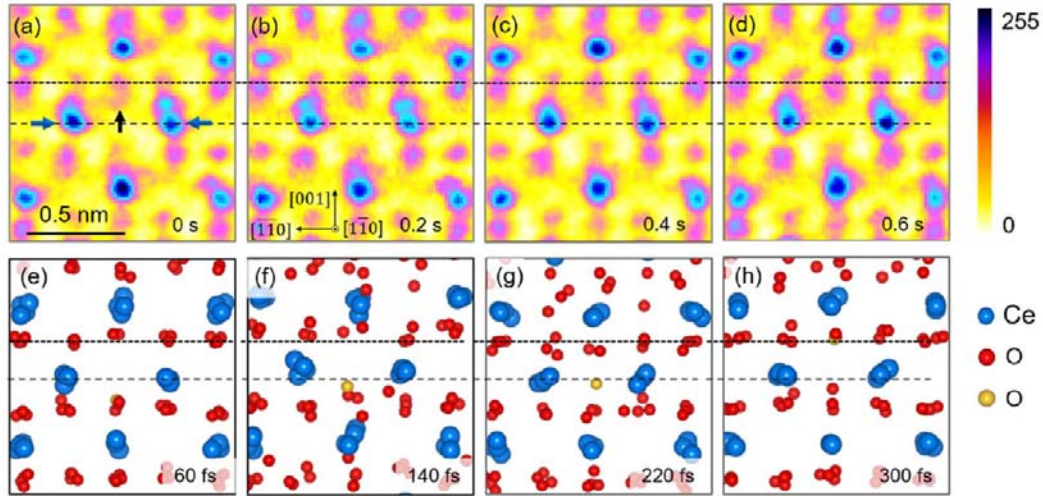


FIG. 2. The interplay between Ce atom arrangement and oxygen vacancy diffusion. (a)–(d) Sequential TEM images showing rearrangement of Ce and O layers along the [001] crystallographic direction. TEM images are colored for clarity and their contrast is inverted. Blue spots with a high density represent Ce column positions. Pink spots with a low intensity show O column positions.  $t=0$  s is the starting time for the real-time recording. (e)–(h) Snapshots of *ab initio* molecular dynamics simulation. Blue and red atoms represent Ce and O atoms, respectively. Yellow atoms are diffusing O atoms.

response of Ce sub-lattice would be minimized, leading to an anisotropic diffusion of O atoms in ceria.

To get a better understanding of oxygen diffusion process in  $\text{CeO}_2$  during the reduction process, we performed *ab initio* molecular dynamics (MD) simulations. A model structure with half  $\text{CeO}_2$  and half  $\text{Ce}_2\text{O}_3$  was firstly constructed to simulate the interface of the  $\text{CeO}_2$  reduction process (see Fig. 4 in Supplementary Materials [14] for the structure employed in MD simulation). This model is more energetically favorable than structures with a random O vacancy distribution. An MD simulation at 2000 K was carried out and the resulting snapshots are shown in Figs. 2(e)–(h). The diffusion of O atoms along the [001] direction was observed (illustrated by the motion of the yellow ball). During the O atom diffusion process, the related Ce plane splits in the oxygen-diffusion direction (Figs. 2(f) and 2(g)) and becomes flat again at the end of the process (sparse dashed line in MD snapshots, Figs. 2(e)–2(h)). MD calculations are in nice agreement with the experimental findings, further revealing the interplay between O atom diffusion and out-of-plane buckling of Ce lattices.

We then further studied the dynamic behavior of the (001), (110), and (111) surfaces during the reduction to evaluate the

diffusion path of O atoms. Figure 3 displays comparisons of the atomic configurations of the three exposed low-index surfaces with distinct deformation features during the structural transition. For the (001) surface, frequent events of atom diffusion into the vacuum (more than 20 recorded) were recognized, demonstrating that the (001) ceria surface has a very high activity (see video in Supplementary Materials [14]). Figures 3(a) and 3(b) show representative sequential images of the (001) surface during the reduction. The surface was flat and was mostly defined by Ce atom column layers. The two yellow arrows indicate the position of two Ce spots, while the outmost O atoms are highlighted by the green arrow. With the ongoing of the reduction process, the marked O atoms escaped from the crystal. Simultaneously, the distance between the two adjacent Ce atoms increased by  $\sim 10\%$  which is ascribed to the local enhanced Coulomb interaction [8,39]. The dynamics of O atom diffusion and local Ce atom response is illustrated by the schematic in Fig. 3(c). In addition, although the O atom diffusion path in the bulk  $\text{CeO}_2$  is hard to be identified, the observed continuous O atom-releasing events along the [001] direction at (001) surface not only prove the high activity of the (001) plane, but also indicate the preferential diffusion

path of O atoms. As discussed previously, such anisotropic diffusion phenomena could be attributed to the varying local lattice perturbation corresponding to the charge redistribution.

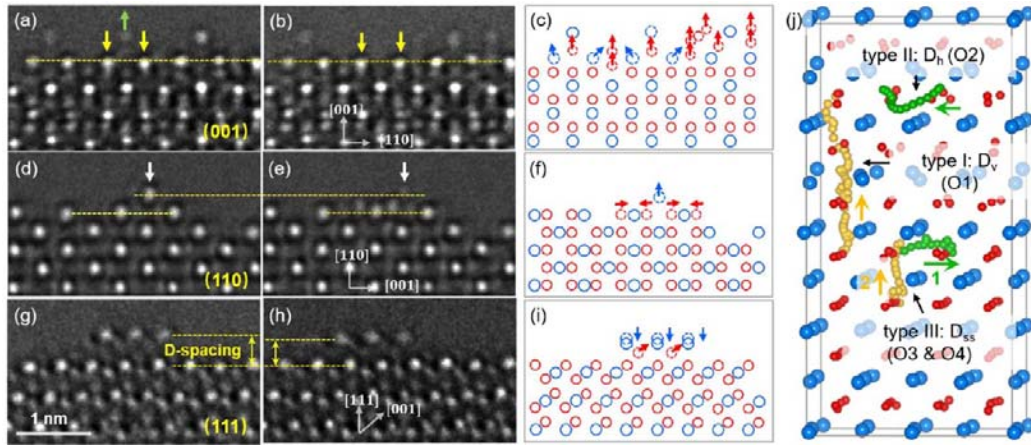


FIG. 3. Low-index surface dynamics in ceria under reduction. (a), (b) TEM image snapshots of the (100) surface. (c) Atomic configuration derived from video data. Blue and red circles represent Ce columns and O positions, respectively. (d), (e) Serial TEM images of the (110) surface flattening under reduction. (f) Atomic configuration derived from (d)–(e). (g), (h) TEM images of the (111) surface linear defect formation. (i) Atomic configuration derived from (g)–(h). (j) Ab initio molecular dynamics simulation calculated trajectory of diffusing O atoms (O1–O4) with three types of diffusion processes.

direction on the surface was easily established, as shown in Figs. 3(d)–(f). In sharp contrast to the (001) and (110) surfaces, after the examination of tens of nanoparticles no apparent atom migration or surface reconstruction were observed on the O-terminated (111) surface, demonstrating the highly robust atomic configuration. On Ce-terminated (111) surfaces [41–43], instead of the independent diffusion of single atoms, collective behavior involving planar O atoms has been recorded (Figs. 3(g)–(h)). Fig. 3(g) shows a small bump of Ce atoms that was occasionally found on the (111) surface keeping a certain plane distance (D-spacing) for storing O atoms. During the reduction process, the D-spacing decreases with the escaping of one oxygen atomic layer. The most probable scenario for the collective release of oxygen atoms on the Ce-terminated (111) surface is the surface reconstruction induced by the polar nature and instability [44].

We further analyzed the MD results, and three types of oxygen atom diffusion processes were identified (see Fig. 5 in the Supplementary Materials [14] for details). The motion trajectory of one O atom is highlighted in Fig. 3(j). The first type is denoted by  $D_v$ , in which O atoms start from the  $\text{CeO}_2$

Contrary to the (001) facet, (110) surface shows much lower O atom diffusion activity [40]. O atoms escaping into the vacuum were barely observed, while migration along the

[ 0 0 1 ]

part and diffuse along the [001] direction. In the second diffusion process, O atoms diffuse into the coplanar neighboring vacancy site, which is denoted by  $D_h$ . Here, O atoms will not diffuse from the  $\text{CeO}_2$  regime to the  $\text{Ce}_2\text{O}_3$  regime, thus contributing little to the reduction of  $\text{CeO}_2$ . The third type is the step-by-step diffusion, denoted by  $D_{ss}$ .  $D_{ss}$  consists of two sequential processes. First, an O atom (represented by O3) diffuses into a coplanar neighboring vacancy site, which creates a vacancy at its original location. Then, an O atom located in the next layer (represented by O4) diffuses along the [001] direction and fills the vacancy created by the O3 diffusion. Furthermore, the energy barrier for O atom diffusion was calculated (see Fig. 6 in Supplementary Materials [14]). An O atom will overcome a barrier of 0.74 eV in  $D_v$ , which is comparable to previously reported experimental results [45]. O atoms diffuse in the equivalent  $\langle 001 \rangle$  direction in all three types of diffusion paths. Therefore, the three types of diffusion paths revealed by the simulation are consistent with our experimental findings that O prefers to diffuse in the  $\langle 001 \rangle$  direction.

The electron energy loss spectroscopy (EELS) measurement of the Ce and O spectra, which reflects the

average valency properties and chemical bonding, are also recorded during the structural phase transition (Fig. 4). The Ce spectra feature two sharp and strong peaks located at 883 and 901 eV, corresponding to the  $M_5$  and  $M_4$  edges, respectively. The two peaks originate from the transition of

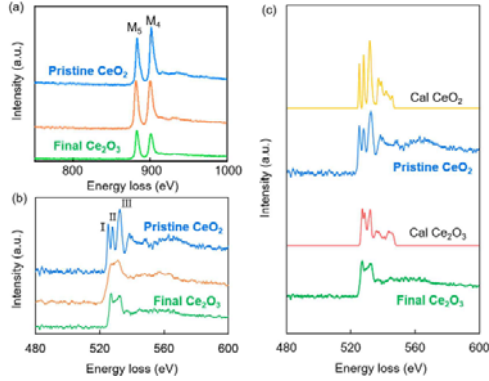


FIG. 4. Intermediate chemical bonding states revealed by electron spectroscopy. (a) Ce M-edge evolution during CeO<sub>2</sub> reduction process. (b) O K-edge evolution during CeO<sub>2</sub> reduction process. (c) Simulated EELS spectra compared with experimental data. Yellow and red curves are calculated O K-edge EELS spectra for CeO<sub>2</sub> and Ce<sub>2</sub>O<sub>3</sub>, respectively.

with previously reported values [36].

The evolution of O K-edge is shown in Fig. 4(b). Pristine oxygen K-edge for CeO<sub>2</sub> has three main peaks marked by □, □, and □. The spectrum for Ce<sub>2</sub>O<sub>3</sub> shows two of these characteristic peaks with a slight peak shift and variation in relative intensities [15]. Peak □ originates from the O-1s electron transition to the p-like component of the hybrid Ce 4f and O 2p states, suggesting an unoccupied 4f state which is characteristic of tetravalent Ce. Peaks □ and □ arise because of the hybridization of unoccupied O 2p-like states with the crystal-field split Ce 5d-e<sub>g</sub> and Ce 5d-t<sub>2g</sub> states, representing a strong local atomic arrangement influence of CeO<sub>8</sub> or CeO<sub>6</sub> [47]. After the structure transition, all three peaks become broader, while contribution of peak □ increases significantly with reduction, leading to a different shape which is supported by the simulations result as shown in Fig. 4(c). The highly dynamic diffusion of O atoms not only gives rise to the accompanying local Ce lattice distortion, but also the non-saturated chemical bonding due to transient non-stoichiometric configurations.

In summary, visualization of O atoms and real-time motion tracking by the aberration-corrected TEM demonstrated the

electrons from the spin-orbit split levels  $3d_{5/2}$  and  $3d_{3/2}$  to the unoccupied 4f states [46]. The  $M_4/M_5$  intensity ratio decreases from 1.12 to 0.75, with an increase in concentration of trivalent Ce depending on the valence state of Ce, which is in agreement preferred <001> diffusion path in ceria, which was verified by DFT calculation and MD simulations. The attendant effects from O atom diffusion, including the neighboring Ce out-of-plane buckling and the variation of the chemical bonding, were demonstrated, describing barriers for the O atom diffusion. The perturbation response of Ce lattice has an anisotropic character, suggesting a micro-mechanism for the anisotropic oxygen diffusion activities. When considering that the interaction between cation ions and oxygen atoms is similar in fluorite-structure oxides, here the newly established mechanism for the oxygen diffusion in ceria further implies that the accompanying response of local cation atoms may be universal, leading to the same anisotropic oxygen diffusion behaviors in other functional fluorite-structure oxides.

This work was supported by the National Natural Science Foundation (11974388, 11974001, 51872284, U1932153, 21872172, 21773303, and 51421002), the National Key R&D Program (2016YFA0300804, 2016YFA0300903, 2018YFA0305800, 2019YFA0307801, and 2019YFA0308500), the Program from Chinese Academy of Sciences (ZDYZ2015-1, Y8K5261B11, XDB30000000, XDB28000000, and XDB07030100), and Beijing Natural Science Foundation (2192022, Z190011). This work, including Argonne Chromatic Aberration-corrected TEM, was performed at the Center for Nanoscale Materials, an Office of Science user facility, supported by the U.S. Department of Energy, Office of Science under Contract No. DE-AC02-06CH11357.

\*L. Z. and J. X. contributed equally to this work.

†zhangyuyang@ucas.ac.cn,

‡leiliu1@pku.edu.cn;

§xdbai@iphy.ac.cn;

¶jwen@anl.gov;

¶¶wanglf@iphy.ac.cn.

- [1] L. Nie, D. Mei, H. Xiong, B. Peng, Z. Ren, X. I. P. Hernandez, A. Delariva, M. Wang, M. H. Engelhard, and L. Kovarik, *Science* **358**, 1419 (2017).
- [2] Q. Fu, H. Saltsburg, and M. Flytzani-Stephanopoulos,

- Science **301**, 935 (2003).
- [3] J. A. Farmer and C. T. Campbell, Science **329**, 933 (2010).
- [4] R. Farrauto, S. Hwang, L. Shore, W. Ruettinger, J. Lampert, T. Giroux, Y. Liu, and O. Ilinich, Annu. Rev. Mater. Res. **33**, 1 (2003).
- [5] E. P. Murray, T. Tsai, and S. A. Barnett, Nature **400**, 649 (1999).
- [6] C. T. Campbell and C. H. F. Peden, Science **309**, 713 (2005).
- [7] Z.-P. Liu, S. J. Jenkins, and D. A. King, Phys. Rev. Lett. **94**, 196102 (2005).
- [8] F. Esch, S. Fabris, L. Zhou, T. Montini, C. Africh, P. Fornasiero, G. Comelli, and R. Rosei, Science **309**, 752 (2005).
- [9] N. V. Skorodumova, S. I. Simak, B. I. Lundqvist, I. A. Abrikosov, and B. Johansson, Phys. Rev. Lett. **89**, 166601 (2002).
- [10] T. W. Hansen, J. B. Wagner, P. L. Hansen, S. Dahl, H. Topsøe, and C. J. H. Jacobsen, Science **294**, 1508 (2001).
- [11] P. A. Crozier and T. W. Hansen, MRS Bull. **40**, 38 (2015).
- [12] H. Topsøe, J. Catal. **216**, 155 (2003).
- [13] C. L. Jia, M. Lentzen, and K. Urban, Science **299**, 870 (2003).
- [14] See Supplemental Material for a discussion of the Materials and Methods, HRTEM image calculation to compare with experimental images, intensity profiles of dynamic O in ceria, evaluation of the Column interactions within the atoms in ceria during oxygen diffusion, the structure employed in MD simulation, evolution of the fractional coordinate of four representative O atoms in MD simulation, oxygen diffusion process in partially reduced CeO<sub>2</sub>, combinations of O K-edge EELS spectra of initial and final state for comparison with intermediate state, O atom diffusion in 1000 K ab initio MD simulation, and real-time TEM video of ceria nanoparticle under the reduction processes, which includes Refs. [15-34].
- [15] M. Nolan, S. C. Parker, and G. W. Watson, Surf. Sci. **595**, 223 (2005).
- [16] O. Kraynis, J. Timoshenko, J. Huang, H. Singh, E. Wachtel, A. I. Frenkel, and I. Lubomirsky, Inorg. Chem. **58**, 7527 (2019).
- [17] G. Kresse and J. Furthmuller, Comp. Mater. Sci. **6**, 15 (1996).
- [18] G. Kresse and J. Hafner, Phys. Rev. B **47**, 558 (1993).
- [19] G. Kresse and J. Hafner, Phys. Rev. B **48**, 13115 (1993).
- [20] P. E. Blochl, Phys. Rev. B **50**, 17953 (1994).
- [21] J. P. Perdew, K. Burke, and M. Ernzerhof, Phys. Rev. Lett. **77**, 3865 (1996).
- [22] S. L. Dudarev, G. A. Botton, S. Y. Savrasov, C. J. Humphreys, and A. P. Sutton, Phys. Rev. B **57**, 1505 (1998).
- [23] M. Nolan, S. Grigoleit, D. C. Sayle, S. C. Parker, and G. W. Watson, Surf. Sci. **576**, 217 (2005).
- [24] D. A. Andersson, S. I. Simak, B. Johansson, I. A. Abrikosov, and N. V. Skorodumova, Phys. Rev. B **75**, 035109 (2007).
- [25] N. Daelman, M. Capdevila-Cortada, and N. Lopez, Nat. Mater. **18**, 1215 (2019).
- [26] S. Nose, Mol. Phys. **52**, 255 (1984).
- [27] S. Nose, J. Chem. Phys. **81**, 511 (1984).
- [28] Y. S. Su and S. T. Pantelides, Phys. Rev. Lett. **88**, 165503 (2002).
- [29] T. J. Pennycook, M. J. Beck, K. Varga, M. Varela, S. J. Pennycook, and S. T. Pantelides, Phys. Rev. Lett. **104**, 115901 (2010).
- [30] G. Henkelman and H. Jonsson, J. Chem. Phys. **113**, 9978 (2000).
- [31] G. Henkelman, B. P. Uberuaga, and H. Jonsson, J. Chem. Phys. **113**, 9901 (2000).
- [32] R. Buczko, G. Duscher, S. J. Pennycook, and S. T. Pantelides, Phys. Rev. Lett. **85**, 2168 (2000).
- [33] W. Luo, M. Varela, J. Tao, S. J. Pennycook, and S. T. Pantelides, Phys. Rev. B **79**, 052405 (2009).
- [34] K. Kambe, G. Lehmpfuhl, F. Fujimoto, and Z. Naturforsch, **29a**, 1034 (1974).
- [35] I. Riess, R. Koerner, M. Ricken, and J. Noelting, Solid State Ionics **28**, 539 (1988).
- [36] M. Romeo, K. Bak, J. El Fallah, F. Le Normand, and L. Hilaire, Surf. Interface Anal. **20**, 508 (1993).
- [37] V. Piacente, G. Bardi, L. Malaspina, and A. Desideri, J. Chem. Phys. **59**, 31 (1973).
- [38] M. Nolan, J. E. Fearon, and G. W. Watson, Solid State Ionics **177**, 3069 (2006).
- [39] H. Y. Li, H. F. Wang, X. Q. Gong, Y. L. Guo, Y. Guo, G. Z. Lu, and P. Hu, Phys. Rev. B **79**, 193401 (2009).
- [40] J. Kullgren, K. Hermansson, and C. Castleton, J. Chem.

Phys. **137**, 044705 (2012).

[41] Y. Namai, K. Fukui, and Y. Iwasawa, *J. Phys. Chem. B* **107**, 11666 (2003).

[42] Y. Namai, K. Fukui, and Y. Iwasawa, *Catal. Today* **85**, 79 (2003).

[43] Y. Lin, Z. Wu, J. Wen, K. R. Poepelmeier, and L. D. Marks, *Nano Lett.* **14**, 191 (2013).

[44] C. Yang, X. Yu, S. Heißler, A. Nefedov, S. Colussi, J. Llorca, A. Trovarelli, Y. Wang, and C. Wöll, *Angew. Chem. Int. Ed.* **56**, 375 (2017).

[45] H. Tuller and A. Nowick, *J. Phys. Chem. Solids* **38**, 859 (1977).

[46] L. Douillard, M. Gautier, N. Thromat, M. Henriot, M. J. Guittet, J. P. Duraud, and G. Tourillon, *Phys. Rev. B* **49**, 16171 (1994).

[47] A. V. Soldatov, T. S. Ivanchenko, S. Della Longa, A. Kotani, Y. Iwamoto, and A. Bianconi, *Phys. Rev. B* **50**, 5074 (1994).